The relative effect of particles and turbulence on acoustic scattering from deep sea hydrothermal vent plumes revisited

Guangyu Xu,[1,a)] Darrell R. Jackson,[2] and Karen G. Bemis[3]

[1]*Woods Hole Oceanographic Institution, Woods Hole, Massachusetts 02543, USA*
[2]*Applied Physics Laboratory at University of Washington, Seattle, Washington 98105, USA*
[3]*Department of Marine and Coastal Sciences at Rutgers University, New Brunswick, New Jersey 08901, USA*

The relative importance of suspended particles and turbulence as backscattering mechanisms within a hydrothermal plume located on the Endeavour Segment of the Juan de Fuca Ridge is determined by comparing acoustic backscatter measured by the Cabled Observatory Vent Imaging Sonar (COVIS) with model calculations based on *in situ* samples of particles suspended within the plume. Analysis of plume samples yields estimates of the mass concentration and size distribution of particles, which are used to quantify their contribution to acoustic backscatter. The result shows negligible effects of plume particles on acoustic backscatter within the initial 10-m rise of the plume. This suggests turbulence-induced temperature fluctuations are the dominant backscattering mechanism within lower levels of the plume. Furthermore, inversion of the observed acoustic backscatter for the standard deviation of temperature within the plume yields a reasonable match with the *in situ* temperature measurements made by a conductivity-temperature-depth instrument. This finding shows that turbulence-induced temperature fluctuations are the dominant backscattering mechanism and demonstrates the potential of using acoustic backscatter as a remote-sensing tool to measure the temperature variability within a hydrothermal plume. © 2017 Acoustical Society of America. [http://dx.doi.org/10.1121/1.4974828]

[APL]   Pages: 1446–1458

I. INTRODUCTION

Seafloor hydrothermal circulation, occurring mainly at oceanic spreading centers, forms conduits connecting the Earth interior and the overlying ocean. Geothermally heated seawater exits the seafloor at hydrothermal vents forming buoyant plumes that rise hundreds, and occasionally, thousands of meters above. The heat and chemicals carried by hydrothermal plumes are important components of the energy and chemical cycles of the global ocean (Bickle and Elderfield, 2004; German and Damm, 2006). Furthermore, the reduced gases carried by hydrothermal plumes fuel chemosynthetic microbes that form the base of lush benthic fauna in vent fields (Govenar, 2012).

Underwater acoustics, as an important remote-sensing tool of oceanographic research, has been applied in many hydrothermal studies (Di Iorio *et al.*, 2005; Rona *et al.*, 2006; Xu *et al.*, 2014; Bemis *et al.*, 2015). In these studies, researchers apply active acoustic techniques (e.g., acoustic scintillation and acoustic imaging) to acquire quantitative information (e.g., flow rate, heat transport, and areal distribution) of hydrothermal discharge by analyzing the scattered acoustic signals. The resultant acoustic measurements have the advantages of having no instrumental interference and large spatial scales relative to the data obtained using conventional instruments.

Acoustics is an effective tool for studying hydrothermal plumes because the plumes are strong sound scatterers.

However, the existence of more than one potential scattering mechanism within a plume (e.g., particles, temperature, or salinity fluctuations) complicates the study of the scattered acoustic signals. While previous studies have investigated sound scattering from plume particles and temperature fluctuations separately (Palmer and Rona, 1986; Goodman *et al.*, 1992; Oeschger and Goodman, 1996, 2003), their combined effects and relative importance have been ignored in most studies. Understanding the relative importance of different scattering mechanisms within a hydrothermal plume is important for the selection of appropriate acoustic models that can transform the existing acoustic techniques to tools of remote sensing of the properties of the suspended particles and temperature/salinity fluctuations within the plume. The dominance of temperature fluctuations within a hydrothermal plume as a scattering mechanism has been previously asserted by Xu and Di Iorio (2011), with strong observational evidence in the case of forward scattering. However, their result is inconclusive for backward scattering due to the lack of contemporaneous acoustic backscatter observation and direct measurements of particle grain size.

In this study, we reconsider the relative importance of backscattering from particles and temperature fluctuations by theoretically estimating the acoustic backscatter from suspended particles based on *in situ* measurements of particle grain size and mass concentration. We then compare the theoretical estimate with the acoustic backscatter recorded by the Cabled Observatory Vent Imaging Sonar (COVIS) to determine the relative contribution of particles to acoustic backscatter from a hydrothermal plume. Furthermore, we

a)Electronic mail: gxu@whoi.edu

explore the potential of inverting backscatter data to obtain information about the temperature fluctuations within a hydrothermal plume.

II. DATA COLLECTION

A. Acoustic imaging of hydrothermal plumes

The idea of acoustic imaging of hydrothermal plumes stems from the detection of plumes as sonar targets during a seafloor terrain survey at the East Pacific Rise (Palmer and Rona, 1986). During the following decades, acoustic imaging has come a long way from being a tool of visualizing hydrothermal plumes to a quantitative means of estimating multiple plume properties (e.g., radius, flow rate, volume transport, and heat transport) (Bemis *et al.*, 2015). COVIS is an innovative sonar system designed to image and quantitatively monitor seafloor hydrothermal plumes (Bemis *et al.*, 2015). In September 2010, COVIS was connected to the Ocean Networks Canada's NEPTUNE observatory to monitor the hydrothermal discharge from the Grotto mound, a hydrothermal sulfide structure on the Endeavour Segment of the Juan de Fuca Ridge in the Northeast Pacific (Bemis *et al.*, 2015; Rona and Light, 2011). The primary component of COVIS is a state-of-the-art imaging sonar, a variant of the Seabat 7125 developed by Reson, Inc. The sonar has two transmitting/receiving pairs: a 396 kHz pair used in imaging and Doppler modes for 3-D plume imaging and flow rate quantification, respectively, and a 200 kHz pair used in diffuse-flow mode for 2-D mapping of lower-temperature hydrothermal discharge (i.e., diffuse flow).

The sonar data presented in this paper were recorded primarily in imaging mode. In this mode, COVIS scans the hydrothermal discharge from Grotto every three hours. During each scan, the 396 kHz transmitter-receiver pair on COVIS first rotates upward from 19° to 59° above the horizontal plane and then downward to the initial position in 1° increments. The combination of the upward and downward rotation processes is called a "sweep," and covers a 40-m thick portion of the water column immediately above the Grotto North Tower. At each 1° step in the upward and downward halves of a total sweep, the transmitter-receiver pair stops to transmit a "burst" of 6 pulses having rectangular envelopes with 0.5 ms pulse width at a source level of 220 dB 1 μPa @ 1 m at a rate of 2 pulses per second. The outputs of the 256 receiver-array elements are digitized and saved as complex "baseband" time series with magnitude equal to the echo signal envelope and phase equal to instantaneous echo signal phase. Data are recorded out to a slant range of 75 m away from the sonar. In later processing, beamforming using a Hamming window provides a "fan" composed of 256 beams with 0.5° 3-dB width covering a sector of angular width 128°. The width in elevation is set by the source and is 1°. The source level, receiver sensitivity, and beam patterns were measured at the Applied Physics Laboratory-University of Washington (APL-UW) acoustic calibration facility. Owing to the relatively large apertures of the source and receiver arrays, corrections were made to compensate for near-field effects. The baseband, beam-formed time series are multiplied by a range-dependent factor such that their average squared magnitude is equal to the volume scattering cross section per unit solid angle per unit volume or volume backscattering coefficient (s_v), having units m^{-1}. Finally, s_v is interpolated onto a uniform 3-D grid with 0.25 m spacing. The gridded data can be expressed in dB as volume backscattering strength ($S_v = 10 \log_{10} s_v$) and visualized to produce 3-D plume images (Fig. 1).

B. Plume particle samples

In order to estimate the contribution of suspended particles to the backscatter signals recorded by COVIS, we need to know the grain size distribution and mass concentration of the suspended particles within the plumes above Grotto. In May 2014, water samples were taken from the major plume above the North Tower of Grotto (the larger plume in Fig. 1, which we call the North Tower plume hereafter) at approximately 1 m above source vents using Niskin bottles carried by the remotely operated vehicle (ROV) ROPOS. The plume samples were filtered aboard through two pre-weighed 0.2 μm Isopore filters and six 0.02 μm Anodisc filters. The particle mass concentration (M) was calculated as the weight increase of each of the two Isopore filters divided by the volume of filtered hydrothermal fluid (1 L). The results are $M = 2.6$ and 5.6 mg/L, respectively.

In order to estimate the particle size distribution, we took microscopic photos of the particle-laden Anodisc filters using a field emission scanning electron microscope (FESEM). Figure 2 shows an example of those FESEM photos. In this photo, the majority of particles have radii $\ll 1 \mu$m, and aggregate to form a layer of "mud cake" that covers almost the entire filter [Fig. 2(b)]. Larger particles ($>1 \mu$m) are found on top of this mud cake layer with far smaller quantities. The particles composing the mud cake appear to have radii smaller than 0.05 μm. Their prevalence in our plume samples
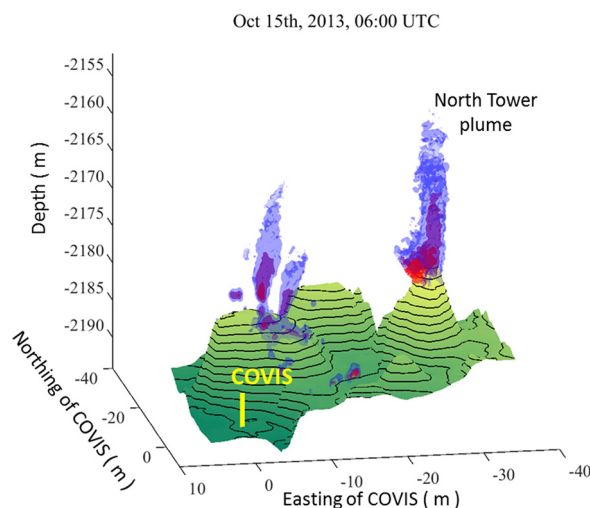
Oct 15th, 2013, 06:00 UTC

FIG. 1. (Color online) 3-D image of the black-smoker plumes above the bottom topography of Grotto (contours in 1 m intervals) produced by processing the COVIS imaging data collected on October 15th, 2013 at 06:00 UTC time. The bathymetric data used to produce the bottom topography was collected during an AUV survey in 2008 (Clague *et al.*, 2008; Clague *et al.*, 2014). The yellow bar marks the location of COVIS. The isosurfaces of the plumes correspond to volume backscattering strength (S_v) as −50 dB (red), −60 dB (magenta), −70 dB (blue).

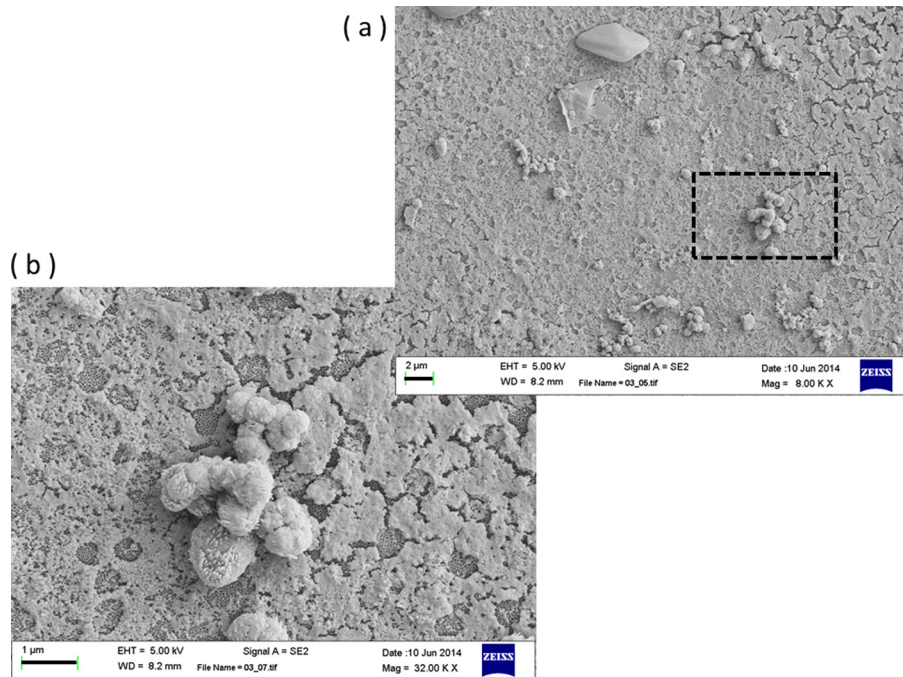J. Acoust. Soc. Am. **141** (3), March 2017

Xu *et al.* 1447

FIG. 2. (Color online) FSEM photos of the suspended particles within the major buoyant plume above the Grotto mound obtained by filtering plume water samples. (a) Large particles (grain size $>1\,\mu m$) underlaid by the aggregate of small particles (grain size $\ll 1\,\mu m$) covering almost the entire filter surface. (b) A close up of the area within the rectangle in (a).

is consistent with a previous finding that nanoparticles (i.e., particles with one or more dimensions less than $0.1\,\mu m$ in size) are a widespread component of high-temperature hydrothermal discharges (Gartman et al., 2014).

In practice, we used image-processing software IMAGEJ to size and count individual particles and particle aggregates that can be clearly distinguished in FESEM photos. Those particles are in general larger than $0.2\,\mu m$. We neglected the particles composing the mud cake because their dense aggregation makes it impossible to distinguish them from one another. Following the procedures detailed in supplementary material,[1] we obtained the probability density function (PSD) of particle size distribution shown in Fig. 3. Table I defines mathematical symbols used and gives values of constant parameters in this paper.
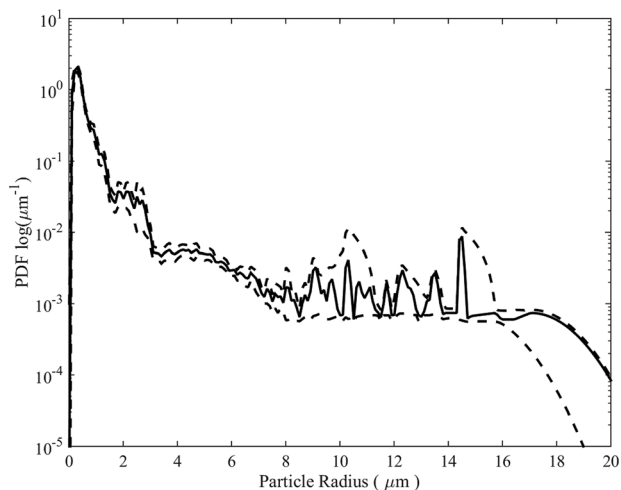

FIG. 3. Probability density function (PDF) of particle size distribution over the size range $0.01 \le a \le 20\,\mu m$. The solid curve is the mean PDF and the dashed curves delimit the 95% confidence interval (see supplementary material for the procedures used to obtain the PDF and its confidence interval). The effective mean grain size corresponding to the mean PDF is $a_0 = 0.75\,\mu m$.

C. *In situ* temperature measurement

We conducted *in situ* temperature measurements within the North Tower plume using a conductivity-temperature-depth instrument (CTD, Seabird 19plusV2) mounted on ROV ROPOS to obtain ground-truth for acoustically obtained plume temperature fluctuations. We conducted a total of six CTD profiles during the same ROV dive where the plume particle samples were collected. During each profile, the ROV first entered the plume at approximately 1 m above the source vents. The ROV adjusted its position within the plume until the real-time temperature reading from the CTD reached a maximum—an indicator that the CTD is at or close to the plume centerline. The ROV then slowly ascended to 15 m above the vents and then descended back to the starting level in the same manner. We grouped the data recorded in the six profiles into 0.5-m vertical bins. We then estimated the plume centerline temperature and its standard deviation as the mean and standard deviation of the highest 10% of the temperature samples in each bin, which were assumed to be taken at or near the plume's centerline.

III. THEORETICAL ESTIMATIONS OF ACOUSTIC BACKSCATTER

A. Individual particles

Mathematical formulas used to quantify the combined backscatter from individual particles have been developed and applied in many previous studies (Sheng and Hay, 1988; Thorne et al., 1993; Thorne and Meral, 2008; Xu and Di Iorio, 2011). Applying the single scattering approximation and the Rayleigh scattering theory gives the combined backscatter from individual particles as

$$s_{vp} = \langle |A_s(a)|^2 \rangle \left(\frac{3M}{4\pi \rho_s \langle a^3 \rangle} \right). \tag{1}$$

TABLE I. Symbols and values of parameters.

Symbol	Description	Values and Units
A_s	Backward scattering amplitude of a particle	m
a	Particle grain size	m
a_0	Mean particle grain size	m
a_T	Fractional change in sound speed due to temperature change	$2.5 \times 10^{-3}\ °\mathrm{C}^{-1}$
b_e	Plume e-folding radius	m
C	Fundamental constant in the 3-D spatial spectrum	1.542
c	Sound speed	1500 m/s
e	Ratio of particle bulk modulus to seawater bulk modulus	40
f_0	Central frequency of COVIS	396 kHz
h	Ratio of particle density to seawater density	4
$\kappa_{B\xi}$	Batchelor wavenumber of acoustic impedance fluctuations	
$\kappa_{B\xi}$	Batchelor wavenumber of thermal diffusion	
κ_v	Kolmogorov wavenumber	
k_0	Sonar wavenumber of COVIS	$1.7 \times 10^3\ \mathrm{rad/m}$
k_T	Molecular thermal diffusivity	$1.5 \times 10^{-7}\ \mathrm{m^2/s}$
K_L	Wavenumber corresponding to the largest eddies within the plume	6.3 rad/m
M	Particle mass concentration	$\mathrm{kg/m^3}$
$n(a)$	Probability density function (PDF) of the particle size distribution	$\mathrm{m^{-1}}$
q	Straining constant	3.7
W	Plume centerline vertical flow rate	m/s
z	Height above the source vents	m
α	Entrainment coefficient	
α_T	Thermal expansion coefficient	$1.3 \times 10^{-4}\ °\mathrm{C}^{-1}$
β	Fractional volume of the plume occupied by particles	
$\overline{\beta'^2}$	Variance of β	
ϵ	Turbulent kinetic energy dissipation rate	W/kg
χ_ξ	Acoustic impedance variance dissipation rate	$\mathrm{s^{-1}}$
$\overline{T'^2}$	Variance of plume temperature	$°\mathrm{C^2}$
ρ_0	Reference density	$1000\ \mathrm{kg/m^3}$
ρ_w	Density of seawater	$1028\ \mathrm{kg/m^3}$
ρ_s	Particle density	$4000\ \mathrm{kg/m^3}$
S_v	Volume backscattering strength	dB
s_v	Volume backscattering coefficient	$\mathrm{m^{-1}}$
s_{vp}	Contribution of individual particles to s_v	
s_{vm}	Contribution of particle microstructure to s_v	
s_{vT}	Contribution of temperature fluctuations to s_v	
ξ	Normalized acoustic impedance fluctuations	
σ_ξ	Standard deviation of ξ	
μ	Dynamic viscosity of plume fluid	$10^{-3}\ \mathrm{Pa\ s}$
ν	Kinematic viscosity of plume fluid	$10^{-6}\ \mathrm{m^2/s}$

The derivation of Eq. (1) and justifications of the underlying assumptions are given in Appendix A. Within Eq. (1), s_v is the volume backscattering coefficient in units m^{-1} (i.e., backscattering cross-section per unit solid angle per unit volume), and the subscript p refers to individual particles; $|A_s(a)|^2$ is the squared backward scattering amplitude of a particle, which is proportional to the sixth power of particle radius (a) in the Rayleigh scattering regime (Palmer, 1996), M is the particle mass concentration in units $\mathrm{kg/m^3}$, and ρ_s is the mass density of a single particle. The angular brackets represent an average over the particle size distribution

$$\langle |A_s(a)|^2 \rangle = \int_0^\infty |A_s(a)|^2 P(a)\, da, \tag{2}$$

$$\langle a^3 \rangle = \int_0^\infty a^3 P(a)\, da, \tag{3}$$

where $P(a)$ is the PDF of particle size distribution.

B. Microstructure within particle suspension

Aside from individual particles, the turbulence-induced microstructure in the spatial distribution of particles is another source of acoustic backscatter (Appendix B). Flows are generally considered as fully turbulent if the Reynolds number (Re) satisfies $Re > 10^4$. The Reynolds number of a buoyant plume can be calculated as

$$Re = \frac{W_0 b_e \rho}{\mu}, \tag{4}$$

where W_0 is the plume's centerline vertical flow rate, b_e is the plume's e-folding radius (i.e., the distance from the plume's centerline to where the plume's vertical flow rate decreases to $1/e$ or 37% of W_0), ρ is the density of plume fluid, and μ is the dynamic viscosity of the plume fluid. Processing COVIS Doppler-mode data recorded in May 2014 gives $0.15 \leq W \leq 0.25$ m/s and $1 \leq b_e \leq 3$ m over the initial 10-m rise of the North Tower plume (Fig. 8). Substituting these along with $\rho = 1000$ kg/m^3 and $\mu = 10^{-3}$ Pa s gives $2.5 \times 10^5 \leq R_e \leq 4.5 \times 10^5$. Thus the North Tower plume can be regarded as fully turbulent.

The turbulent microstructure of plume particles leads to fluctuations of the density of plume fluid and thus its acoustic impedance, which in turn scatter sound waves. The resulting volume backscatter coefficient is

$$s_{vm} = \frac{q\nu^{1/2}\overline{\beta'^2}H\kappa_L^{2/3}k_0}{24\epsilon^{1/6}C}\exp\left(-qK^2/\kappa_v^2\right) \qquad (5)$$

with

$$H = \frac{1}{4}\left[\frac{3(h-1)}{1+2h} - \frac{1}{e} + 1\right]^2.$$

The derivation of Eq. (5) is given in Appendix B. Within Eq. (5), the subscript m refers to microstructure in particle spatial distribution; $\beta = M/\rho_s$ is the fractional volume of the plume occupied by particles, and $\overline{\beta'^2}$ is its variance; H is a factor dependent on the elastic properties of particles including $e = K_s/K_w$, the ratio of particle bulk modulus (K_s) to seawater bulk modulus (K_w), and $h = \rho_s/\rho_w$, the ratio of particle density (ρ_s) to seawater density (ρ_w); $\kappa_L = 2\pi/L$ is the wavenumber corresponding to the outer scale of the inertial-convective subrange, in which $L = 2b_e$; $k_0 = 2\pi f_0/c$ is the wavenumber associated with the acoustic signals used in the imaging and Doppler modes of COVIS where $f_0 = 396$ kHz is the sonar frequency and $c = 1500$ m/s is the sound speed; ϵ is the turbulent kinetic energy dissipation rate (see Appendix B for the estimation of ϵ); $K = 2k_0$ is the Bragg wavenumber; $\kappa_v = (\epsilon/(\nu^3))^{1/4}$ is the Kolmogorov wavenumber where ν is the kinematic viscosity; C is a fundamental constant determined by Ross (2003) to be 1.542; $q = 3.7$ is the straining constant (Oakey, 1982).

C. Temperature fluctuations

The same turbulence responsible for the presence of microstructure in particle spatial distribution also causes fluctuations in the temperature, salinity, and velocity fields within the plume. These fluctuations lead to variations of density and sound speed, which in turn scatter sound waves.

According to Di Iorio *et al.* (2005), the sound-scattering effect of salinity variations in a hydrothermal plume is small compared to that of temperature variations. Additionally, turbulent velocity has zero effect on backward scattering (Ross, 2003). This is because turbulent velocity contributes to sound scattering through its impact on the effective sound speed. However, the net effect is zero for backward scattering since the change of effective sound speed is canceled out

exactly for the incident and scattered sound waves combined. Therefore, we neglect the effects of salinity and velocity fluctuations on backscatter in this study.

The volume scattering coefficient of the turbulence-induced temperature fluctuations is

$$s_{vT} = \frac{q\nu^{1/2}\overline{T'^2}(a_T - \alpha_T)^2\kappa_L^{2/3}k_0}{96\epsilon^{1/6}C}\exp\left(-qK^2/\kappa_{BT}^2\right). \qquad (6)$$

The derivation of Eq. (6) is given in Appendix B. Within Eq. (6), the subscript T refers to temperature fluctuations, $\overline{T'^2}$ is the variance of temperature fluctuations, a_T is the fractional change in sound speed due to temperature change, α_T is the thermal expansion coefficient, and $\kappa_{BT} = (\epsilon/(\nu k_T^2))^{1/4}$ is the Batchelor wavenumber where k_T is the molecular diffusivity of heat.

IV. RESULTS AND DISCUSSION

A. Relative importance of particles to acoustic backscatter

To estimate the combined acoustic backscatter from individual particles, we substitute the two measured mass concentrations M and the PDF of the particle size distribution estimated from the samples taken from the North Tower plume (Fig. 3) into Eqs. (1)–(3) and solve the integral numerically (the upper limit of the integral is set to be $500\,\mu$m). The resulting volume backscattering strength is $S_v = -85$ dB for $M = 2.6$ mg/L, and $S_v = -82$ dB for $M = 5.6$ mg/L. The uncertainty of the PDF, quantified as its 95% CI, results in a 0.5 dB error in S_v. In addition, we assume the standard deviation of M equals 50% of the mean, which leads to a 1.8 dB error in S_v. As a result, the combined uncertainty in particle size distribution and mass concentration leads to an error in S_v of $0.5 + 1.8 = 2.3$ dB. It should be noted that the oxidative dissolution and precipitation of particles in the Niskin bottles during the time period between sample collection and recovery (several hours) and during the filtration process (a couple of hours) introduce inherent uncertainty in the estimated particle size distribution and mass concentration, which subsequently leads to an additional error in S_v. This error is neglected based on the assumption that the effect of oxidative dissolution and precipitation on particle mass concentration and size distribution is insignificant.

In addition to the combined backscatter from individual particles, we estimate the backscatter from the microstructure in particle spatial distribution using Eq. (5). Assuming $\sqrt{\overline{\beta'^2}}$ equals one-fourth of the mean value of β and applying the values of constant parameters listed in Table I gives $S_v = -131$ dB for $M = 6$ mg/L. Note that this estimate is much smaller than the estimate of the combined backscatter from individual particles (~-80 dB). This suggests the backscatter from the microstructure in particle spatial distribution is negligible compared with the combined backscatter from individual particles.

Figure 4 shows the backscatter measured by COVIS over a horizontal cross-section of the North Tower plume at approximately 1 m above the source vents, which is approximately the same level where the plume samples were taken.
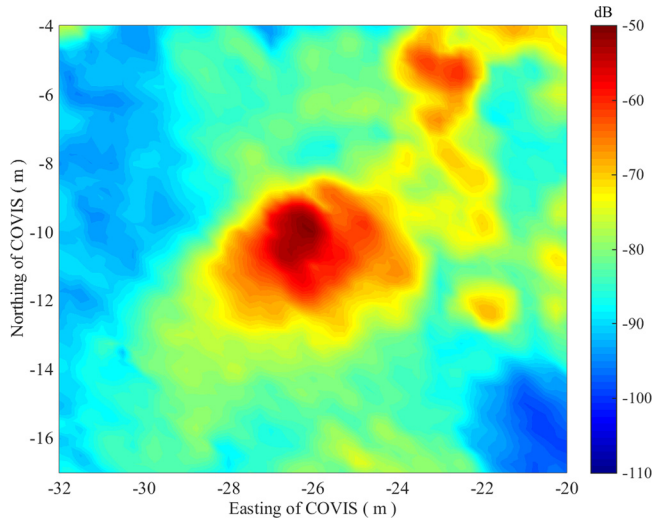
FIG. 4. (Color online) Volume backscattering strength (S_v) measured by COVIS over the horizontal cross-section of the North Tower plume at 1 m above the source vents. The acoustic measurement, conducted on May 20th, 2014 at 15 h UTC, preceded the collection of plume particle samples by 3 h.

FIG. 5. Comparison of estimated volume backscattering strength (S_v) from plume particles as a function of the height above the source vents (z) (solid curve) with observed backscatter. The particle size distribution used in the estimation is obtained from the particle samples taken at 1 m above the source vents (Fig. 3), which is assumed to be invariant with height. The particle mass concentration used in the estimation follows the $<100\,\mu m$ curve in Fig. 6. The gray shaded area marks the 2.3 dB error in S_v as discussed at the beginning of Sec. IV A. The dot-dashed and dashed curves and shaded areas denote the means and standard deviations of the COVIS measurements of S_v at the plume centerline and boundary, respectively, over the month of May in 2014.

The corresponding acoustic dataset was recorded no more than 3 h before the collection of plume samples. Figure 4 shows $S_v > -60$ dB close to the center of the plume, which is more than two orders of magnitude higher than the estimated backscatter from particles (~ -80 dB). Equation (1) suggests the combined backscatter from individual particles is proportional to their mass concentration $s_v \sim M$. Therefore, in order for the backscatter from particles to reach the observed level, one needs a particle mass concentration two orders of magnitude higher than the measurement: that is, the observed backscatter intensity predicts a particle concentration of $M \sim 600$ mg/L for the estimated particle size distribution ($a_0 \sim 0.75\,\mu m$) shown in Fig. 3. Note that hydrothermal plumes with much higher particle mass concentrations and/or mean particle sizes may exist elsewhere. For example, Mottl and McConachy (1990) reported a particle mass concentration of $M \sim 2000$ mg/L for a plume on the East Pacific Rise (EPR) near 21°N. In this case, based on the earlier discussion, the contribution of plume particles to acoustic backscatter may no longer be negligible.

For the acoustic backscatter at heights beyond 1 m above the source vents, the 3-D acoustic backscatter data recorded by COVIS suggests a general decrease with height (Fig. 5). Within Fig. 5, the dot-dashed curve shows the estimated S_v at the centerline of the North Tower plume as a function of the height above the source vents (z). Using the method described in Xu et al. (2013), we estimate the centerline value of S_v at a given height by fitting a 2-D Gaussian curve to the measured horizontal cross-section of S_v at that height and taking the peak value of the Gaussian curve. The dashed curve in Fig. 5 shows the estimated S_v at the plume boundary, which is defined as $1/\exp(2) \approx 14\%$ of the corresponding centerline estimate. The general decrease in backscatter with height shown in Fig. 5 is expected because both the temperature fluctuations and particle concentration reduce as the plume gets increasingly diluted during its buoyant rise by mixing with ambient seawater.
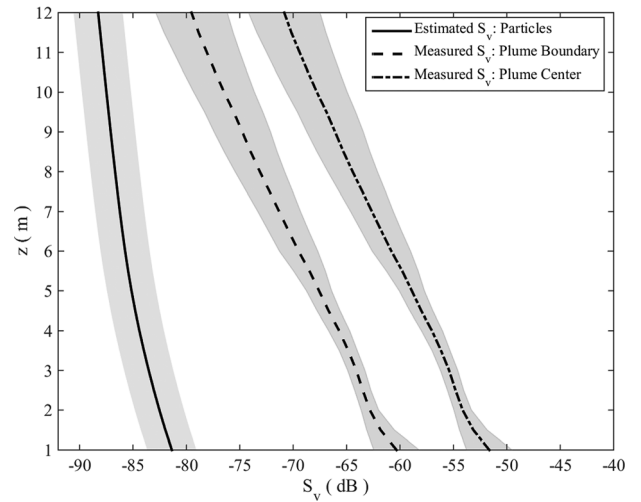
Estimating the contribution of particles to the acoustic backscatter observed at levels higher than 1 m above the source vents requires knowledge of the particle mass concentration (M) and size distributions at those levels. In Appendix C, we develop a formula for estimating the variation of M with height for particles having a given radius. The formula is based on the classic particle sedimentation theory described in Bursik et al. (1992), Ernst et al. (1996), and Bemis et al. (2006), which uses the plume flow rate and radius estimated by processing COVIS Doppler-mode data along with a given initial value of $M = 6$ mg/L at $z = 1$ m as the input data. The results shown in Fig. 6 exhibit a general decrease in M with height, and the slope of the decrease increases with increasing particle grain size. The decrease of M with height is due to both the dilution of the plume as it mixes with ambient seawater and the fallout of particles through the plume's lateral and bottom boundaries. The fallout of particles accelerates with increasing particle size and so does the decrease in M with height. In the absence of particle fallout, the decrease of M with height is a sole result of plume dilution and is thus independent of particle size. In this case, all the curves in Fig. 6 would overlap, which is the case for particles smaller than $100\,\mu m$. This suggests the vertical flows within the plume are strong enough to carry particles up to $100\,\mu m$ through the initial 12 m rise. Since the vast majority of the particles observed in the samples collected from the North Tower plume are well below $100\,\mu m$, it is sensible to assume the particle fallout is negligible and the predicted variation of M with height to follow the $<100\,\mu m$ curve in Fig. 6. Similarly, it is reasonable to assume particle size distribution to be invariant through the initial 12 m plume rise.
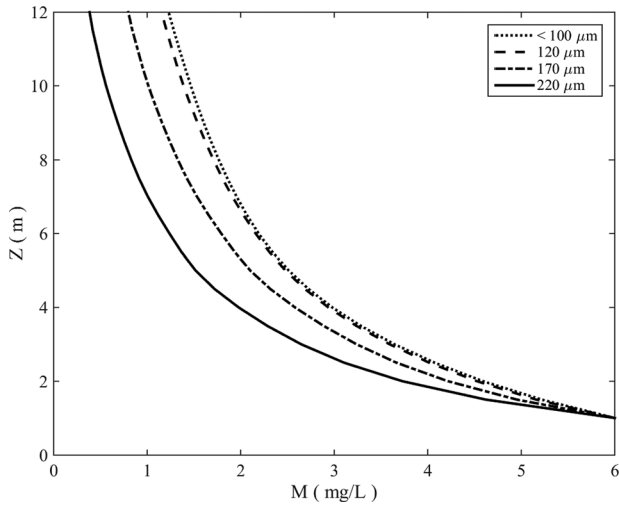
FIG. 6. Predicted variation of particle mass concentration (M) as a function of height above the source vents (z) estimated using the formula described in Appendix C for different particle grain sizes. The plume vertical flow rate and radius used in the calculation are averaged over the COVIS Doppler data recorded in May 2014. The initial value of M at $z = 1$ m is 6 mg/L.

Substituting the predicted particle mass concentration (M) obtained above and the probability density function (PDF) of particle size distribution estimated from plume particle samples (Fig. 3) into Eq. (1) gives the estimated variations of volume backscattering strength (S_v) with height in Fig. 5. The result suggests the estimated particle-generated backscatter is ubiquitously lower than the measurements. The predicted volume scattering coefficient due to particles is approximately 1% of the measurement at the plume boundary at $z = 1$ m and this percentage increases to 13% at $z = 12$ m. This result suggests the relative importance of plume particles to acoustic backscatter increases with height, which is apparent in Fig. 5 as the estimated backscatter from particles decreases from height more slowly than the measurements. This result implies the contribution of particles to acoustic backscatter could be significant at higher levels of the plume ($z \gg 10$ m).

B. Estimation of temperature variability from acoustic backscatter

The discussion in the preceding section suggests the contribution of particles to the acoustic backscatter recorded by COVIS from the initial tens-of-meter rise of the North Tower plume is negligible. This finding, on the other hand, suggests the temperature fluctuations are the dominant scattering mechanism causing the backscatter signals received by COVIS. As a result, it is sensible to assume temperature fluctuations to be the only backscattering mechanism. Under this assumption, one can invert the acoustic backscatter to obtain estimates of the temperature fluctuations within the plume using Eq. (6). In practice, we substitute the observed centerline volume backscattering strength (S_v) shown in Fig. 5 along with the values of ε and b_e (used to calculate κ_L) shown in Fig. 8 into Eq. (6) to estimate the corresponding centerline temperature standard deviation ($\sqrt{\overline{T'^2}}$). The values of the constant parameters used in the calculation are given in Table I.
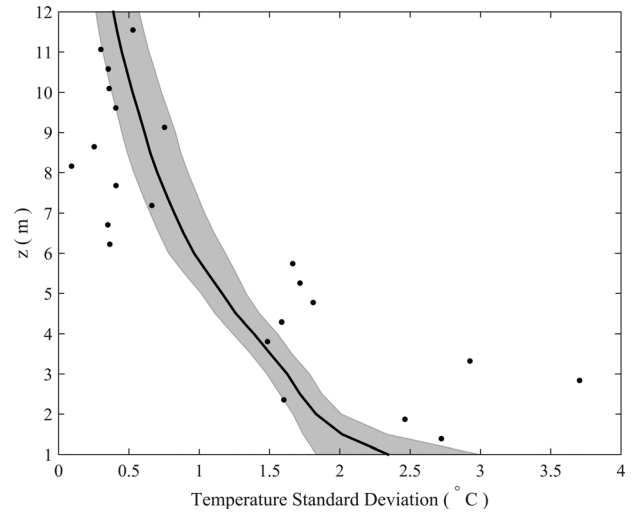

FIG. 7. Comparison of acoustically estimated plume centerline temperature standard deviation ($\sqrt{\overline{T'^2}}$) (black curve) with observations (dots). The acoustic estimates are obtained from the observed acoustic backscatter along the centerline of the North Tower plume (Fig. 5). The gray shade marks the uncertainty in the acoustic estimates caused by the uncertainty in the observed backscatter. The observed $\sqrt{\overline{T'^2}}$ is estimated from the CTD data recorded on the same ROV dive on which the plume particle samples were taken.

Figure 7 shows the acoustically estimated $\sqrt{\overline{T'^2}}$ and its comparison with the $\sqrt{\overline{T'^2}}$ estimated from the *in situ* temperature measurements made within the North Tower plume (Sec. II C). The comparison exhibits a reasonable match with the CTD measurements having a slightly steeper decrease
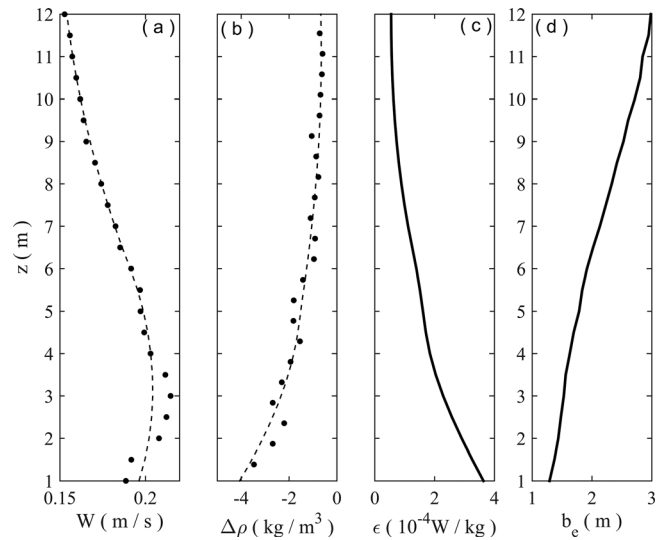

FIG. 8. (a) Mean vertical flow rate (W_0) along the centerline of the North Tower plume as a function of the height above the source vents (z) (dots). The estimates of W_0 are obtained by processing the Doppler-mode data recorded by COVIS in May 2014 following the procedures described in Xu *et al.* (2013) and taking the monthly average. The dashed curve denotes the smoothed estimates obtained using a LOESS filter. (b) Mean centerline density difference between the plume and the ambient seawater ($\Delta \rho$) estimated from the CTD data recorded during the same ROV dive on which the plume particle samples were collected (dots). The dashed curve denotes the smoothed estimates obtained using a LOESS filter. (c) Turbulent kinetic energy dissipation rate (ϵ) calculated from the estimates of W_0 and $\Delta \rho$ using Eqs. (B4)–(B6). (d) Plume e-folding radius (b_e) obtained by processing the Doppler-mode data recorded by COVIS in May 2014 following the procedures described in Xu *et al.* (2013) and taking the monthly average.

with height than the acoustic estimates. The reasonable fit in Fig. 7 corroborates the idea that turbulence-induced temperature fluctuations are the dominant mechanism causing the acoustic backscatter from the initial 10-m rise of the North Tower plume. It also demonstrates the potential of using acoustic backscatter as a remote sensing tool to measure the temperature fluctuations within a hydrothermal plume.

V. CONCLUSIONS

In this study, we investigate the relative importance of particles and temperature fluctuations as backscattering mechanisms within a hydrothermal plume based on *in situ* plume particle samples and near-contemporaneous acoustic backscatter measurements made by an imaging sonar. We estimate the size distribution and mass concentration of plume particles by analyzing the *in situ* particle samples. The estimated size distribution suggests the number of particles with radii much smaller than $1\,\mu m$ far exceeds the number of larger particles. The theoretically estimated backscatter from plume particles based on their estimated size distribution and mass concentration is approximately two orders of magnitudes smaller than the observed backscatter. This finding suggests turbulence-induced temperature fluctuations, rather than plume particles, are the dominant backscattering mechanism during the initial ten-meter rise of the plume. However, the relative contribution of plume particles to acoustic backscatter increases with height and can possibly be significant at higher levels of the plume. We invert the measured acoustic backscatter to obtain estimates of the temperature standard deviations within the plume, which exhibit a reasonable match with CTD measurements. This finding corroborates the idea that temperature fluctuations are the dominant backscattering mechanism and demonstrates the potential of using acoustic backscatter as a remote-sensing tool to measure the temperature variability within a hydrothermal plume.

APPENDIX A: BACKSCATTER FROM INDIVIDUAL PARTICLES

The acoustic backscatter from a particulate suspension can be estimated as the sum of intensities of backscatter from individual particles if multiple scattering is neglected—the single scattering approximation. This approximation is valid under the condition (Ishimaru, 1978)

$$s_{vt}\Delta r \ll 1, \tag{A1}$$

where s_{vt} is the total volume scattering coefficient of the particulate suspension and Δr is the distance traveled by the sound signal through the suspension. Assuming that the sound scattering from the suspension is isotropic, it follows that

$$s_{vt} = 4\pi s_v, \tag{A2}$$

where s_v is the volume backscattering coefficient (i.e., backscattering cross-section per unit solid angle per unit volume). According to Fig. 4, COVIS measurements suggest $S_v = 10\log_{10}s_v \sim -50$ dB at the center of the North Tower plume at $1\,m$ above the source vents. Substituting this value into Eqs. (A2) and (A1) and taking $\Delta r = 4\,m$ [the mean diameter of the plume within its initial 10-m rise (Xu *et al.*, 2013)] gives $s_{vt}\Delta r \approx 5\times 10^{-4}$. Therefore, the condition for neglecting multiple scattering is well satisfied.

Applying the single scattering approximation, the volume backscattering coefficient of the particulate suspension is defined as (Medwin and Clay, 1998)

$$s_{vp} = N\langle |A_s(a)|^2 \rangle. \tag{A3}$$

Within Eq. (A3), N is the number of particles per unit volume of the suspension; $|A_s(a)|^2$ is the squared single-particle backscattering amplitude, which is a function of particle radius (a); $\langle\,\rangle$ is the average over the particle size distribution as defined in Eq. (2).

The Rayleigh scattering theory applies for particles whose grain sizes are sufficiently small such that $k_0a \ll 1$, where $k_0 = 2\pi f_0/c$, f_0 and c are the central frequency of the sonar and sound speed, respectively. For COVIS $f_0 = 396\,kHz$, and taking $c = 1500\,m/s$ gives $k_0 = 1.66\times 10^3$ rad/s. Therefore, the Rayleigh scattering theory is applicable for $a \ll 1/k_0 = 603\,\mu m$, which is well satisfied given the size distribution estimated from the particle samples taken from the North Tower plume, Eq. (A2). According to Palmer (1996), the squared backward scattering amplitude averaged over particle shape and orientation within the Rayleigh scattering regime is

$$|A_s(a)|^2 = \frac{k_0^3 a^6}{9}\left\{ \left(\frac{e-1}{e} + \frac{h^2-1}{2h}\right)^2 + \frac{1}{20}\frac{(h-1)^4}{h^2} \right\}. \tag{A4}$$

Within Eq. (A4), $e = K_s/K_w$ is the ratio of particle bulk modulus (K_s) to seawater bulk modulus (K_w); $h = \rho_s/\rho_w$ is the ratio of particle density (ρ_s) to seawater density (ρ_w). The particle mass concentration (in units kg/m^3) can be expressed as

$$M = \frac{4\pi\rho_s}{3}N\langle a^3\rangle, \tag{A5}$$

where $\langle a^3\rangle$ is defined in Eq. (3). Substituting Eq. (A5) in Eq. (A3) to eliminate N gives

$$s_{vp} = \langle|A_s(a)|^2\rangle\left(\frac{3M}{4\pi\rho_s\langle a^3\rangle}\right) \tag{A6}$$

which is Eq. (1) in Sec. III A.

APPENDIX B: BACKSCATTER FROM TURBULENCE

Turbulence-induced microstructure in the spatial distribution of plume particles and temperature fluctuations lead to fluctuations of the acoustic impedance, which in turn scatter sound waves. The relevant volume backscattering coefficient (s_v) can be expressed in terms of the 3-D spatial spectrum of the fluctuations of acoustic impedance as

$$s_v = 2\pi k_0^4 \Phi_\xi(K)|_{\kappa=2k_0}. \tag{B1}$$

Within Eq. (B1), $\Phi_\xi(K)$ is the 3-D spatial spectrum of the normalized acoustic impedance fluctuations ξ (i.e., fluctuations of acoustic impedance divided by its mean) evaluated at the Bragg wavenumber $K = 2k_0$ assuming ξ is statistically homogeneous and isotropic; $k_0 = 2\pi f_0/c$, where f_0 and c are the central frequency of the sonar and sound speed, respectively. According to Ross (2003), the 3-D spatial spectrum of fully-developed, homogeneous, isotropic turbulence has the form

$$\Phi_\xi(K) = \frac{C}{2\pi\epsilon^{1/3}}\frac{\chi_\xi}{2}K^{-11/3} \tag{B2}$$

in the inertial-convective subrange [$\kappa_L \leq K \leq (5/12)^{3/2}\kappa_v$, where κ_L is the wavenumber corresponding to the outer scale of the inertial-convective subrange and κ_v is the Kolmogorov wavenumber]. In the viscous-convective subrange [$\kappa_{B\xi} > K > (5/12)^{3/2}\kappa_v$], the 3-D spatial spectrum has the form

$$\Phi_\xi(K) = \frac{q\nu^{1/2}}{2\pi\epsilon^{1/2}}\frac{\chi_\xi}{2}K^{-3}\exp\left(-qK^2/\kappa_{B\xi}^2\right). \tag{B3}$$

Within Eqs. (B2) and (B3), C is a fundamental constant whose value is determined by Ross (2003) to be 1.542, $q = 3.7$ is the straining constant, ϵ is the turbulent kinetic energy dissipation rate, χ_ξ is the acoustic impedance variance dissipation rate, $\kappa_v = (\epsilon/\nu^3)^{1/4}$ is the Kolmogorov wavenumber and ν is the kinematic viscosity of plume fluid, and $\kappa_{B\xi} = (\epsilon/(\nu k_\xi^2))^{1/4}$ is the Batchelor wavenumber associated with acoustic impedance whose molecular diffusivity is k_ξ. Assuming the molecular diffusion of acoustic impedance is dominated by thermal diffusion gives $\kappa_{B\xi} \approx \kappa_{BT} = (\epsilon/(\nu k_T^2))^{1/4}$, where $k_T = 1.5 \times 10^{-7}$ m^2/s is the molecular thermal diffusivity.

Selecting the right form of $\Phi_\xi(K)$ [either Eq. (B2) or (B3)] requires knowledge of κ_v, which further requires knowing ϵ. Since there is no direct measurement of the turbulence within the North Tower plume, we estimate ϵ from the turbulent kinetic energy budget [modified from the original equations in Gregg (1987)]

$$-\langle w'w'\rangle\frac{dW}{dz} = \langle\rho'w'\rangle\frac{g}{\rho_0} + \epsilon, \tag{B4}$$

where w' and W are the turbulent and mean plume vertical flow rate, ρ' and ρ_0 are the density fluctuations and reference density of the plume, g is the gravitational acceleration, and $\langle\,\rangle$ denotes ensemble average. The laboratory results reported in Wang and Law (2002) suggest the ratios of turbulent to mean transport are constant at the centerline of a buoyancy-driven plume,

$$\frac{\sqrt{\langle w'w'\rangle}}{W} = 6.83\%, \tag{B5}$$

$$\frac{\langle w'\rho'\rangle}{W\Delta\rho} = 5.09\%, \tag{B6}$$

where $\Delta\rho$ is the mean density difference between the plume and the ambient seawater. In practice, we estimate W along the centerline of the North Tower plume from the Doppler-mode data recorded by COVIS following the procedures described in Xu et al. (2013) [Fig. 8(a)]. We estimate $\Delta\rho$ as $\Delta\rho = \rho_0\alpha_T\Delta T$, where ρ_0 is the reference density, α_T is the thermal expansion coefficient, and ΔT is the difference between the plume centerline temperature and ambient seawater temperature estimated from the conductivity-temperature-depth (CTD) measurements conducted within the North Tower plume during the same ROV dive on which the plume particles samples were collected (see Sec. II C for the details of the CTD data collection and processing). We smooth the estimates of W and $\Delta\rho$ using a LOESS filter [dashed curves in Figs. 8(a) and 8(b)] before substituting them into Eqs. (B5) and (B6) to calculate the turbulent transport terms $\langle w'w'\rangle$ and $\langle w'\rho'\rangle$, which are further substituted into Eq. (B4) to estimate ϵ [Fig. 8(c)].

Figure 9 shows the Kolmogorov wavenumber calculated from the estimated ϵ shown in Fig. 8(c) and $\nu = 1.3 \times 10^{-6}$ m^2/s. Also shown in the figure is the Bragg wavenumber corresponding to the acoustic signals used in the imaging and Doppler modes of COVIS: $K = 2k_0 = 4\pi f_0/c = 3.33 \times 10^3$ rad/s with $f_0 = 396$ kHz and $c = 1500$ m/s. The result suggests $\kappa_{BT} > K > \kappa_v$, and thus the turbulence that is responsible for generating the backscatter is in the viscous-convective subrange. Hence, Eq. (B3) should be used for $\Phi_\xi(K)$.

Calculating the spectrum in Eq. (B3) requires knowledge of the acoustic impedance variance dissipation rate (χ_ξ) within the plume, which is not directly measured. In practice, we estimate χ_ξ from the variance of the normalized acoustic impedance fluctuations (σ_ξ^2) as follows. By definition,

$$\sigma_\xi^2 = 4\pi\int_{\kappa_L}^\infty K^2\Phi_\xi(K)dK, \tag{B7}$$

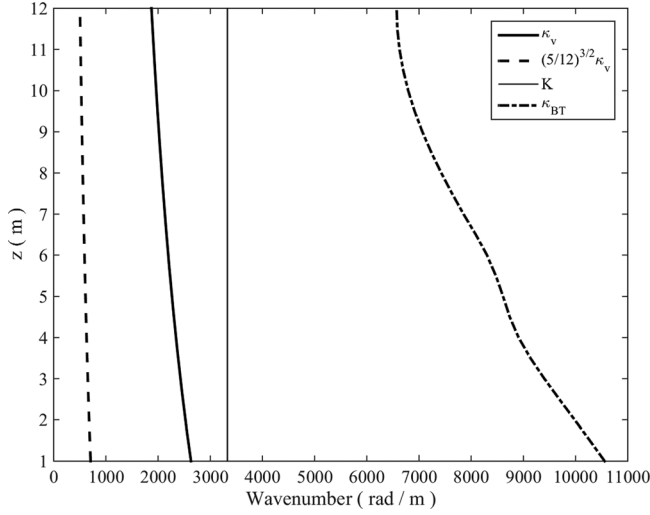1454   J. Acoust. Soc. Am. **141** (3), March 2017

Xu et al.

FIG. 9. The Kolmogorov wavenumber (κ_v) along the centerline of the North Tower plume as a function of the height above the source vents (z) (solid curve), the lower limit of the viscous-convective subrange (dashed curve), the Bragg wavenumber corresponding to the acoustic signals used in the Imaging and Doppler modes of COVIS (thin vertical line), and the Batchelor wavenumber (κ_{BT}) associated with thermal diffusion (dot-dashed curve).

where $\kappa_L = 2\pi/L$ is the wavenumber corresponding to the outer scale (L) of the inertial-convective subrange, and the infinite upper limit suggests the integration is over all turbulence scales $\leq L$. In practice, we determine L as $2b_e$ where b_e is the plume's e-folding radius obtained by processing the Doppler-mode data recorded by COVIS following the procedures described in Xu *et al.* (2013) [Fig. 8(d)].

To simplify the integration, we set the upper limit of the integral to $(5/12)^{3/2}\kappa_v$. This approximation is reasonable since the relative contribution from the eddies in the range $\kappa > (5/12)^{3/2}\kappa_v$ is expected to be small. Substituting Eq. (B2) into Eq. (B7) then gives

$$\sigma_\xi^2 = \frac{3C}{\epsilon^{1/3}} \frac{\chi_\xi}{2} \left(\kappa_L^{-2/3} - \frac{12}{5}\kappa_v^{-2/3} \right)$$
$$\approx \frac{3C}{\epsilon^{1/3}} \frac{\chi_\xi}{2} \kappa_L^{-2/3} \quad \text{for } \kappa_L \ll \kappa_v, \tag{B8}$$

and thus

$$\chi_\xi = \frac{2\epsilon^{1/3}\sigma_\xi^2\kappa_L^{2/3}}{3C}. \tag{B9}$$

Substituting Eqs. (B9) into (B3) gives

$$\Phi_\xi(K) = \frac{q\nu^{1/2}}{2\pi\epsilon^{1/6}} \frac{\sigma_\xi^2\kappa_L^{2/3}}{3C} K^{-3} \exp\left(-qK^2/\kappa_{B\xi}^2\right). \tag{B10}$$

Substituting the equation above into Eq. (B1) gives the volume backscattering coefficient (s_v) of the turbulence-induced acoustic impedance fluctuations

$$s_v = \frac{q\nu^{1/2}\sigma_\xi^2\kappa_L^{2/3}k_0}{24\epsilon^{1/6}C} \exp\left(-qK^2/\kappa_{B\xi}^2\right). \tag{B11}$$

1. Backscatter from microstructure in spatial distribution of particles

The acoustic impedance of particle-loaded seawater is

$$Z = \sqrt{K_e\rho_e}, \tag{B12}$$

where K_e and ρ_e are the effective bulk modulus and density of the particle-loaded seawater. According to Richardson *et al.* (2002),

$$1/K_e = (1 - \beta)/K_w + \beta/K_s, \tag{B13}$$

$$\rho_e = \rho_w \frac{1 - \beta + (2 + \beta)h}{1 + 2\beta + 2(1 - \beta)h}, \tag{B14}$$

where K_w is seawater bulk modulus, K_s is particle bulk modulus, $\beta = M/\rho_s$ is the fractional volume of the suspension occupied by the particles, and $h = \rho_s/\rho_w$ is the ratio of particle density (ρ_s) to seawater density (ρ_w).

Since $\beta \ll 1$, substituting Eqs. (B13) and (B14) into Eq. (B12) and expanding the resulting expression to the first order of β gives

$$Z = Z_w \left\{ 1 + \frac{\beta}{2} \left[\frac{3(h - 1)}{1 + 2h} - \frac{1}{e} + 1 \right] \right\}, \tag{B15}$$

where $Z_w = \sqrt{K_w\rho_w}$ is the acoustic impedance of seawater, $e = K_s/K_w$ is the ratio of particle bulk modulus (K_s) to seawater bulk modulus (K_w). Similarly, the variance of the normalized acoustic impedance fluctuations (σ_ξ^2) approximated to the first order of β is

$$\sigma_\xi^2 = \frac{\overline{(Z - \bar{Z})^2}}{\bar{Z}^2} = \overline{\beta'^2} \frac{1}{4} \left[\frac{3(h - 1)}{1 + 2h} - \frac{1}{e} + 1 \right]^2, \tag{B16}$$

where $\overline{\beta'^2}$ is the variance of β, which increases with increasing magnitude of particle concentration fluctuations. Substituting σ_ξ^2 into Eq. (B11) gives the volume backscattering coefficient of the microstructure in spatial distribution of particles

$$s_{vm} = \frac{q\nu^{1/2}\overline{\beta'^2}H\kappa_L^{2/3}k_0}{24\epsilon^{1/6}C} \exp\left(-qK^2/\kappa_v^2\right) \tag{B17}$$

with

$$H = \frac{1}{4} \left[\frac{3(h - 1)}{1 + 2h} - \frac{1}{e} + 1 \right]^2,$$

which is Eq. (5) in Sec. III B. Note that the use of the Kolmogorov wavenumber (κ_v) instead of the Batchelor wavenumber in the exponent reflects the fact that the microstructure in particle spatial distribution is caused by turbulent velocity as opposed to thermal diffusion.

2. Backscatter from temperature fluctuations

The contribution of temperature fluctuations to σ_ξ^2 can be approximated to the first order as

J. Acoust. Soc. Am. **141** (3), March 2017

Xu *et al.*   1455

$$\sigma_\xi^2 = \frac{1}{4}\overline{T'^2}(a_T - \alpha_T)^2. \tag{B18}$$

Within Eq. (B18), $\overline{T'^2}$ is the variance of temperature fluctuations, a_T is the fractional change in sound speed due to temperature change, and α_T is the thermal expansion coefficient. Substituting Eq. (B18) into Eq. (B11) gives the volume backscattering coefficient of the microstructure temperature field

$$s_{vT} = \frac{q\nu^{1/2}\overline{T'^2}(a_T - \alpha_T)^2 \kappa_L^{2/3} k_0}{96\epsilon^{1/6}C}\exp(-qK^2/\kappa_{BT}^2), \tag{B19}$$

which is Eq. (6) in Sec. III C, where κ_{BT} is the Batchelor wavenumber for thermal diffusion.

APPENDIX C: PARTICLE SEDIMENTATION FORMULATION

Based on the classic sedimentation theories described in Bursik et al. (1992), Ernst et al. (1996), and Bemis et al. (2006), particles are lost from a vertical segment of an axisymmetric plume through the segment's lateral sloping margins and bottom boundary. Additionally, particle fallout from higher levels enters the segment through its top and lateral boundaries. The latter is a result of the re-entrainment caused by the turbulent eddies that sweep ambient seawater into the plume through its lateral boundaries (Fig. 10).

In general, fallout occurs when the particles' terminal settling velocity (v_t) is equivalent to or greater than the plume's vertical flow rate (W). According to Papanicolaou and List (1988), we can assume W to be Gaussian distributed over a given horizontal cross-section of the plume

$$W(r,z) = W_0(z)\exp\left(-\frac{r^2}{b_e^2}\right), \tag{C1}$$

where r is the radial distance from the plume centerline, $W_0(z)$ is the centerline vertical flow rate at a given height z, and b_e is the plume's e-folding radius (i.e., the distance from the plume centerline to where W decrease to $1/e$ of W_0). According to Bonadonna et al. (1998), the expressions of v_t for different particle Reynolds numbers (R_p) are

$$v_t = \left[\frac{3.1g(\rho_s - \rho)2a}{\rho}\right]^{1/2}, \quad \text{for } R_p > 500, \tag{C2}$$

$$v_t = 2a\left[\frac{4(\rho_s - \rho)^2 g^2}{225\mu\rho}\right], \quad \text{for } 0.4 < R_p < 500, \tag{C3}$$

$$v_t = \frac{g(\rho_s - \rho)4R^2}{18\mu}, \quad \text{for } R_p < 0.4, \tag{C4}$$

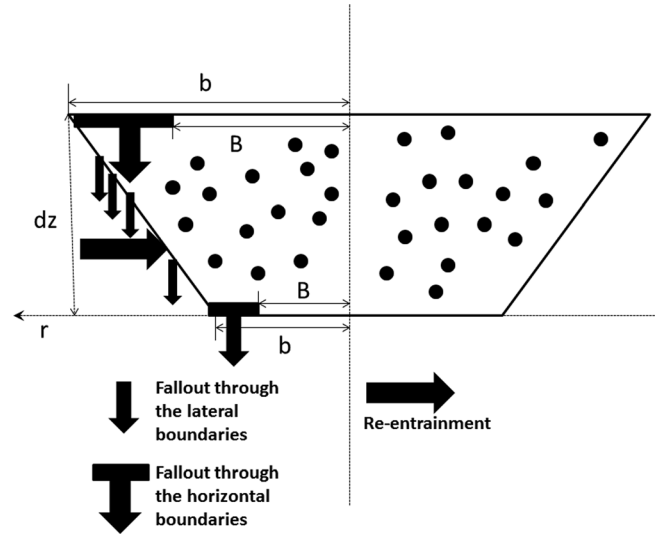where R_p is defined as

$$R_p = 2W_0 a\rho/\mu. \tag{C5}$$

FIG. 10. Conceptual diagram of the particle fallout from and re-entrainment into a vertical segment of an axisymmetric plume of thickness dz. Within the figure, b is the radial distance from the centerline of the plume to its lateral sloping margins and B is the radial distance at which the plume's vertical flow rate equals the particles' terminal settling velocity. The areas from which the particles are lost from the plume segment are the lateral margins and the circular region between B and b on the bottom. Additionally, particles enter the segment through its lateral margins as a result of the re-entrainment effects and through the circular region between B and b on the top boundary. This diagram summarizes the concepts of plume particle sedimentation theories described in Bursik et al. (1992), Ernst et al. (1996), and Bemis et al. (2006).

Within Fig. 10, b is the distance from the centerline of the plume to its lateral boundaries, which is defined as $b = \sqrt{2}b_e$; B is the distance from the centerline to where W equals v_t, which is the radial distance at and beyond which the particle fallout occurs. In the conceptual model depicted in Fig. 10, which follows the plume particle sedimentation theories described in Bursik et al. (1992), Ernst et al. (1996), and Bemis et al. (2006), the loss of particles from a plume segment is restricted to being through the lateral boundaries and the annulus within $B < r < b$ on the bottom. The conservation of the total mass of particles within the segment can be written as

$$\frac{d}{dz}Q = \frac{d}{dz}q - L + R, \tag{C6}$$

where Q is the mass transport of particles across the horizontal boundaries of the segment; q is the mass transport of particles through the annulus within $B < r < b$; Ldz is the mass transport of particles lost through the lateral boundaries; and Rdz is the mass transport of the particles re-entrained into the segment. Assuming the particle mass concentration (M) has the same Gaussian cross-sectional distribution as W gives

$$M(r,z) = M_0(z)\exp\left(-\frac{r^2}{\lambda^2 b_e^2}\right), \tag{C7}$$

where $M_0(z)$ is the particle mass concentration at the centerline of the plume at a given height and λ is the ratio between the e-folding radii of the profiles of M and W. Subsequently, the expressions of Q and q are

$$Q = 2\pi \int_0^b WMr\,dr, \qquad (C8)$$

$$q = 2\pi v_t \int_B^b Mr\,dr. \qquad (C9)$$

According to Bursik *et al.* (1992),

$$Ldz = \eta v_t H, \qquad (C10)$$

where

$$H = 2\pi \int_0^b Mr\,dr \qquad (C11)$$

is the total mass of the particles per unit thickness of the segment; the coefficient η arises from the geometry of the sloping margins of the segment and has the expression

$$\eta = \frac{2(A_t - A_b)}{(A_t + A_b)}. \qquad (C12)$$

Within Eq. (C12), A_t and A_b are the areas of the top and bottom boundaries of the segment, respectively, which can be written as

$$A_t = \pi(b + \tan\phi dz)^2,$$
$$A_b = \pi b^2,$$

where $\tan\phi = db/dz$ is the slope of lateral boundaries. Substituting these expressions into Eq. (C12) and neglecting the second order terms of dz gives

$$\eta \approx 2\tan\phi dz/b. \qquad (C13)$$

Substituting Eqs. (C11) and (C12) into Eq. (C10) gives

$$L = \frac{4\pi \tan\phi}{b} v_t \int_0^b Mr\,dr. \qquad (C14)$$

Adapted from the formula given in Ernst *et al.* (1996), the mass transport of the particles re-entrained into the segment is

$$Rdz = \frac{2\Psi dz H U_e}{b}, \qquad (C15)$$

where Ψ is the re-entrainment coefficient defined in Ernst *et al.* (1996) with an empirically determined value of 0.4 for a buoyant plume; U_e is the flow rate at which the ambient seawater is entrained into the plume. According to Morton *et al.* (1956),

$$U_e = \alpha W_0, \qquad (C16)$$

where α is the entrainment coefficient and is related to the slope of lateral boundaries as $\alpha = 5\tan\phi/6$. Substituting Eq. (C11) into Eq. (C15) gives

$$R = \frac{4\pi \Psi U_e}{b} \int_0^b Mr\,dr. \qquad (C17)$$

Substituting Eqs. (C8), (C9), (C14), and (C17) into Eq. (C6) and eliminating the factor 2π gives

$$\frac{d}{dz}\int_0^b WMr\,dr = \frac{d}{dz}v_t \int_B^b Mr\,dr - \frac{2\tan\phi}{b}v_t \int_0^b Mr\,dr$$
$$+ \frac{2\Psi U_e}{b}\int_0^b Mr\,dr, \qquad (C18)$$

where W, M, and v_t have the expressions given in Eqs. (C1), (C7), and (C4).

Using the method described in Xu *et al.* (2013), we obtain time-series measurements of the centerline vertical flow rate (W_0) and e-folding radius (b_e) of the plume by processing the COVIS Doppler-mode data. In practice, we substitute W_0 and b_e averaged over the time series of May 2014 [Figs. 8(a) and 8(d)] into Eqs. (C1) and (C16) to calculate W and U_e. We then choose a given particle size and calculate the corresponding v_t using Eq. (C4). Finally, we substitute W, U_e, and v_t into and integrate Eq. (C18) from $z = 1$ m to a given height to obtain the centerline mass concentration (M_0) of particles having the chosen grain size at that height. The initial value used in the integration is $M_0 = 6$ mg/L at $z = 1$ m (Fig. 6).

Bemis, K., Silver, D., Rona, P., and Cowen, J. (**2006**). "A particle sedimentation model of buoyant jets: Observations of hydrothermal plumes," Cahiers Biol. Marine **47**, 379–384.

Bemis, K. G., Silver, D., Xu, G., Light, R., Jackson, D., Jones, C., Ozer, S., and Liu, L. (**2015**). "The path to COVIS: A review of acoustic imaging of hydrothermal flow regimes," Deep-Sea Res. Part II **121**, 159–176.

Bickle, M., and Elderfield, H. (**2004**). "Hydrothermal fluxes in a global context," in *Hydrogeology of the Ocean Lithosphere*, edited by E. Davis and H. Elderfield (Cambridge University Press, Cambridge, UK), pp. 677–690.

Bonadonna, C., Ernst, G. G. J., and Sparks, R. S. J. (**1998**). "Thickness variations and volume estimates of tephra fall deposits: The importance of particle Reynolds number," J. Volcanol. Geotherm. Res. **81**, 173–187.

Bursik, M. I., Sparks, R. S. J., Gilbert, J. S., and Carey, S. N. (**1992**). "Sedimentation of tephra by volcanic plumes: I. Theory and its comparison with a study of the Fogo A Plinian deposit, Sao Miguel (Azores)," Bull. Volcanol. **54**, 329–344.

Clague, D. A., Caress, D. W., Thomas, H., Thompson, D., Calarco, M., Holden, J., and Butterfield, D. (**2008**). "Abundance and distribution of hydrothermal chimneys and mounds on the Endeavour Ridge determined by 1-m resolution AUV multibeam mapping surveys," in *EOS, Transactions, American Geophysical Union 89, Fall Meeting*, abstract No. V41B-2079.

Clague, D. A., Dreyer, B. M., Paduan, J. B., Martin, J. F., Caress, D. W., Gill, J. B., Kelley, D. S., Thomas, H., Portner, R. A., Delaney, J. R., Guilderson, T. P., and McGann, M. L. (**2014**). "Eruptive and tectonic history of the Endeavour Segment, Juan de Fuca Ridge, based on AUV mapping data and lava flow ages," Geochem. Geophys. Geosyst. **15**, 3364–3391.

Di Iorio, D., Lemon, D., and Chave, R. (**2005**). "A self-contained acoustic scintillation instrument for path-averaged measurements of flow and turbulence with application to hydrothermal vent and bottom boundary layer dynamics," J. Atmos. Ocean. Technol. **22**, 1602–1617.

Ernst, G. G. J., Sparks, R. S. J., Carey, S. N., and Bursik, M. I. (**1996**). "Sedimentation from turbulent jets and plumes," J. Geophys. Res.—Solid Earth **101**, 5575–5589.

Gartman, A., Findlay, A. J., and Luther, G. W., III (**2014**). "Nanoparticulate pyrite and other nanoparticles are a widespread component of hydrothermal vent black smoker emissions," Chem. Geol. **366**, 32–41.

German, C. R., and Damm, K. L. V. (**2006**). "Hydrothermal processes," in *The Oceans and Marine Geochemistry, Treatise on Geochemistry*, edited by H. Elderfield, H. Holland, and K. Turekian (Pergamon Press, Oxford, UK), Vol. 6, pp. 182–222.

Goodman, L., Oeschger, J., and Szargowicz, D. (**1992**). "Ocean acoustics turbulence study: Acoustic scattering from a buoyant axisymmetric plume," J. Acoust. Soc. Am. **91**, 3212–3227.

Govenar, B. (**2012**). "Energy transfer through food webs at hydrothermal vents: Linking the lithosphere to the biosphere," Oceanography **25**, 246–255.

Gregg, M. C. (**1987**). "Diapycnal mixing in the thermocline: A review," J. Geophys. Res. **92**, 5249–5286, doi:10.1029/JC092iC05p05249.

Ishimaru, A. (**1978**). *Wave Propagation and Scattering in Random Media* (Academic Press, Burlington, MA), Vol. 2, Chap. 4.

Medwin, H., and Clay, C. S. (**1998**). *Fundamentals of Acoustical Oceanography* (Academic Press, San Diego, CA), Chap. 7.

Morton, B. R., Taylor, G., and Turner, J. (**1956**). "Turbulent gravitational convection from maintained and instantaneous sources," Proc. R. Soc. London **234**, 1–23.

Mottl, M. J., and McConachy, T. F. (**1990**). "Chemical processes in buoyant hydrothermal plumes on the East Pacific Rise near 21°N," Geochim. Cosmochim. Acta **54**, 1911–1927.

Oakey, N. S. (**1982**). "Determination of the rate of dissipation of turbulent energy from simultaneous temperature and velocity shear microstructure measurements," J. Phys. Oceanogr. **12**, 256–271.

Oeschger, J., and Goodman, L. (**1996**). "Acoustic scattering from a thermally driven buoyant plume," J. Acoust. Soc. Am. **100**, 1451–1462.

Oeschger, J., and Goodman, L. (**2003**). "Acoustic scattering from a thermally driven buoyant plume revisited," J. Acoust. Soc. Am. **113**, 1353–1367.

Palmer, D. (**1996**). "Rayleigh scattering from nonspherical particles," J. Acoust. Soc. Am. **99**, 1901–1912.

Palmer, D., and Rona, P. (**1986**). "Acoustic imaging of high-temperature hydrothermal plumes at sea floor spreading centers," J. Acoust. Soc. Am. **80**, 888–898.

Papanicolaou, P. N., and List, E. (**1988**). "Investigation of round vertical turbulent buoyant jet," J. Fluid Mech. **195**, 341–391.

Richardson, M. D., Williams, K. L., Briggs, K. B., and Thorsos, E. I. (**2002**). "Dynamic measurement of sediment grain compressibility at atmospheric pressure: Acoustic applications," IEEE J. Ocean. Eng. **27**, 593–601.

Rona, P., and Light, R. (**2011**). "Sonar images hydrothermal vents in seafloor observatory," in *EOS, Transactions, American Geophysical Union*, Vol. 92(20), pp. 169–170.

Rona, P. A., Bemis, K. G., Jones, C. D., and Jackson, D. R. (**2006**). "Entrainment and bending in a major hydrothermal plume, Main Endeavour Field, Juan de Fuca Ridge," Geophys. Res. Lett. **33**, L19313, doi:10.1029/2006GL027211.

Ross, T. (**2003**). "Sound Scattering from Oceanic Turbulence," Ph.D. thesis, University of Victoria, Victoria, British Columbia, Canada.

Sheng, J., and Hay, A. E. (**1988**). "An examination of the spherical scatterer approximation in aqueous suspensions of sand," J. Acoust. Soc. Am. **83**, 598–610.

Thorne, P. D., Manley, C., and Brimelow, J. (**1993**). "Measurements of the form function and total scattering cross section for a suspension of spheres," J. Acoust. Soc. Am. **93**, 243–248.

Thorne, P. D., and Meral, R. (**2008**). "Formulations for the scattering properties of suspended sandy sediments for use in the application of acoustics to sediment transport processes," Cont. Shelf Res. **28**, 309–317.

Wang, H., and Law, A. W.-K. (**2002**). "Second-oder integral model for a round turbulent buoyant jet," J. Fluid Mech. **459**, 397–428.

Xu, G., and Di Iorio, D. (**2011**). "The relative effects of particles and turbulence on acoustic scattering from deep-sea hydrothermal vent plumes," J. Acoust. Soc. Am. **130**, 1856–1867.

Xu, G., Jackson, D. R., Bemis, K. G., and Rona, P. A. (**2013**). "Observations of the volume flux of a seafloor hydrothermal plume using an acoustic imaging sonar," Geochem. Geophys. Geosyst. **14**, 2369–2382.

Xu, G., Jackson, D. R., Bemis, K. G., and Rona, P. A. (**2014**). "Time-series measurement of hydrothermal heat flux at the Grotto mound, Endeavour Segment, Juan de Fuca Ridge," Earth Planet. Sci. Lett. **404**, 220–231.